

ACCEPTED MANUSCRIPT

Full-wave model for the lower hybrid wave electric field vector with synthetic turbulence on Alcator C-Mod

To cite this article before publication: Cornwall Lau *et al* 2019 *Nucl. Fusion* in press <https://doi.org/10.1088/1741-4326/ab6481>

Manuscript version: Accepted Manuscript

Accepted Manuscript is “the version of the article accepted for publication including all changes made as a result of the peer review process, and which may also include the addition to the article by IOP Publishing of a header, an article ID, a cover sheet and/or an ‘Accepted Manuscript’ watermark, but excluding any other editing, typesetting or other changes made by IOP Publishing and/or its licensors”

This Accepted Manuscript is © 2019 IAEA, Vienna.

During the embargo period (the 12 month period from the publication of the Version of Record of this article), the Accepted Manuscript is fully protected by copyright and cannot be reused or reposted elsewhere.

As the Version of Record of this article is going to be / has been published on a subscription basis, this Accepted Manuscript is available for reuse under a CC BY-NC-ND 3.0 licence after the 12 month embargo period.

After the embargo period, everyone is permitted to use copy and redistribute this article for non-commercial purposes only, provided that they adhere to all the terms of the licence <https://creativecommons.org/licenses/by-nc-nd/3.0>

Although reasonable endeavours have been taken to obtain all necessary permissions from third parties to include their copyrighted content within this article, their full citation and copyright line may not be present in this Accepted Manuscript version. Before using any content from this article, please refer to the Version of Record on IOPscience once published for full citation and copyright details, as permissions will likely be required. All third party content is fully copyright protected, unless specifically stated otherwise in the figure caption in the Version of Record.

View the [article online](#) for updates and enhancements.

Full-wave model for the lower hybrid wave electric field vector with synthetic turbulence on Alcator C-Mod

C. Lau^{1, a)}, E.H Martin¹, S. Shiraiwa², G.M Wallace²

¹*Oak Ridge National Laboratory, Oak Ridge, TN, USA*

²*MIT Plasma Science and Fusion Center, Cambridge, MA, USA*

^{a)}lauch@ornl.gov

Abstract: The effects of synthetic turbulence on lower hybrid (LH) wave field magnitude and polarization are studied on Alcator C-Mod. Three synthetic turbulence models are evaluated to assess the impact of filaments, holes, and periodic fluctuations on the LH wave electric fields. For all three cases, the synthetic turbulence can greatly impact the LH wave magnitude and polarization. Back scattering, interference and edge/SOL absorption of the LH wave is observed. This impact is shown to depend on the wavelength and amplitude of the fluctuations. The strongest effect appears for fluctuations at high amplitudes and wavelengths comparable to the LH wavelength. This synthetic turbulence model can be used as inputs into a synthetic diagnostic to calculate the lower hybrid wave field magnitude and direction measured by dynamic Stark effect spectroscopy. It will be shown that fluctuations at these high amplitudes and wavelengths may explain the experimentally measured results. The effect of fluctuations on modifying LH polarization are also shown to be anti-correlated with SOL power losses, similar to recently observed experimental trends on Alcator C-Mod. These SOL losses may have detrimental impact on LHCD efficiency.

1. Introduction

To achieve steady state operation for advanced scenarios in a future fusion reactor, the tokamak reactor concept requires actuators to drive the toroidal current and tailor the toroidal current profile¹⁻³. Lower hybrid (LH) waves are one of the most promising and efficient techniques to drive non-inductive current in tokamaks and have been successfully used on many experiments such as Tore Supra^{4,5}, FTU^{6,7}, Alcator C-Mod^{8,9}, and EAST^{10,11}. One significant challenge with lower hybrid current drive (LHCD), however, is that many of these successful discharges occurred at low line averaged densities^{7,8,11-13}. Scrape-off-layer (SOL) absorption of the LH wave from collisional absorption^{14,15}, parametric decay instabilities¹⁶⁻²³, and/or scattering from density fluctuations²⁴⁻²⁶ have been suggested to explain these results. Relatively efficient LHCD operation have recently occurred at high line averaged densities, likely by mitigating these physical mechanisms^{7,23}.

To understand the importance of these mechanisms and to improve LHCD efficiency, diagnostics and modeling are required. Recent results using a dynamic Stark Effect Lower Hybrid Field (SELHF) diagnostic²⁷ has been used to measure the LH wave electric field vector in the SOL on Alcator C-mod. A synthetic diagnostic has been developed to interpret these measurements. In this paper²⁷, it was shown that there could be agreement between the LH wave magnitude between measurement and simulation within the experimental uncertainty; however, differences between the measurement and simulation for the LH

1
2
3 wave polarization could not be resolved for typical density profiles without fluctuations. This paper focuses
4 in more detail on how density fluctuations can possibly resolve the polarization discrepancies between
5 experiment and simulation.
6

7
8 The paper is organized as follows. Section 2 discusses the SELHF synthetic diagnostic²⁷ in more detail
9 and shows the sensitivity of the simulated LH electric field and polarization to density and collision
10 frequency. Section 2 also discusses the three different synthetic turbulence models (periodic fluctuations,
11 blobs, and holes) used in this paper. This paper then shows three key results. Firstly, the inclusion of
12 poloidally varying density fluctuations with the appropriate amplitude and poloidal wavelength in the model
13 can greatly modify the LH wave propagation and absorption for a range of synthetic turbulence models
14 such as periodic, blobs, and holes. This is shown in section 3. Secondly, the inclusion of synthetic turbulence
15 can allow for the simulation to better match experimental measurement of the LH electric field polarization.
16 This is shown in section 4. Thirdly, the calculated SOL absorption of the LH wave and polarization
17 modification are anti-correlated and may be consistent with observed trends of increasing LH SOL
18 absorption with increasing fluctuation amplitudes²³. This is also shown in section 4. Section 5 discusses the
19 current limitations of the model, possible improvements to the model and conclusions of the paper.
20

21 2. SELHF synthetic diagnostic on Alcator C-Mod

22
23 The SELHF synthetic diagnostic calculates the LH wave electric field vector viewed by the periscope
24 in the SELHF diagnostic on Alcator C-Mod. Section 2 is divided into 4 parts. Section 2.1 discusses the 2-
25 D axisymmetric cold plasma full wave model that forms the key component of the SELHF synthetic
26 diagnostic. Section 2.2 discusses the actual 3-D SELHF synthetic diagnostic that is used to compare with
27 the SELHF experimental measurements. Section 2.3 shows a sensitivity scan of the synthetic diagnostic to
28 uncertainties in density and collision frequency. The insensitivity of the simulated LH polarization to these
29 parameters motivates the need for density fluctuations in the model. Section 2.4 therefore discusses the
30 synthetic turbulence model used as a possible input into the 2-D axisymmetric cold plasma full wave model.
31

32 2.1 2-D cold plasma full wave model

33
34 SELHF²⁸ is a passive polarized optical emission spectroscopy technique to measure the LH electric
35 field magnitude and direction at multiple locations near the 4 rows of the LH launcher²⁹ on Alcator C-Mod.
36 The LH launcher on Alcator C-Mod is a phased waveguide grill with 4 rows and 16 columns. It can operate
37 with up to 2.5 MW of source rf power at 4.6 GHz. The LH power was approximately 300 kW for the
38 experimental discharges used in this paper. SELHF measures the deuterium Balmer line profile and uses a
39 time-periodic Schrodinger equation with the inclusion of a sinusoidal electric field vector to fit the three
40 components of the LH electric field vector. To compare to the measurement, a simulated LH electric field
41 is required. Full wave methods are used here to solve for the LH electric field vector with a plasma dielectric
42 tensor suitable for LH waves. This has previously been done in 2-D^{26,27,30-32} and 3-D^{33,34}. The vector wave
43 equation, shown in equation (1), is solved in 2-D axisymmetric geometry for the LH electric field vector,
44 \vec{E} ,
45

$$46 \nabla \times [\nabla \times \vec{E}_m(r, z)] - \frac{\omega^2}{c^2} [\vec{\epsilon} \cdot \vec{E}_m(r, z)] = 0 \quad (1)$$

47
48 where ω is the LH wave angular frequency, m is the toroidal mode number, $\vec{\epsilon}$ is the cold plasma dielectric
49 tensor³⁵, c is the speed of light, r is the radial coordinate, and z is the vertical coordinate. Measured magnetic
50 field profiles from the magnetic equilibrium reconstruction code, EFIT³⁶, and measured density profiles
51 from a reflectometer³⁷ adjacent to the LH launcher are used as inputs into the cold plasma dielectric tensor³⁷.
52 Collisions are included using a collision frequency term, ν , in the cold plasma dielectric tensor as the only
53
54
55
56
57
58
59
60

absorption mechanism³⁵. In this paper, ν/ω is assumed to be 0.01 for all species and spatially constant for simplicity. It should be noted that this collision frequency is much higher than expected for electron-ion collisions, but it is necessary for two reasons. If the collision frequency is too low, numerical noise prevents the simulation from obtaining meaningful results. Collisions in this model are also used as a proxy for possible deleterious physical mechanisms for LH SOL absorption that could be due to parametric decay, Landau damping of high n_{\parallel} modes, or electron-neutral collisions³⁸. Given that it is unclear how large an effect these physical mechanisms have on the LH SOL losses, a collisional proxy damping mechanism^{39,40} can be used to provide insight into the effect of turbulence on the LH wave propagation. This model certainly has limitations and cannot quantitatively predict SOL losses or the LH electric field magnitude. A sensitivity scan is shown later in this section to estimate the LH electric field uncertainty with respect to the collision frequency.

The toroidal mode number is largely determined by the parallel wavenumber, n_{\parallel} , which can be varied by the LH launcher on Alcator C-Mod. n_{\parallel} is the component of the index of refraction of the launched wave parallel to the magnetic field, and it is an important parameter for LH wave coupling, absorption and current drive⁴¹. For all the 2-D axisymmetric simulations in this paper, $n_{\parallel} = 1.9$, which is the peak n_{\parallel} used for the relevant experiments discussed in this paper. An example 2-D simulation at $n_{\parallel} = 1.9$ is shown in figure 1. Figure 1a) is the input density, which is measured at the outer midplane and assumed to be constant on the magnetic flux surface. Figure 1b) is the output $|\vec{E}|$ and the electric field pattern launched from each of the 4 rows of the LH launcher can be observed. Figure 1c) is the output electric field polarization, θ , that is shown in equation (2). θ is measured in degrees and can be observed to vary as the wave propagates from the SOL to the core of the plasma. There is a high pass $|\vec{E}|$ filter for θ in (2) for two reasons: the SELHF diagnostic has an electric field uncertainty of approximately 5×10^4 V/m and the polarization measured by the diagnostic is strongly biased by the large $|\vec{E}|$. This $|\vec{E}|$ filter also minimizes the noise in the figure where $|\vec{E}| \sim 0$ and the term inside the arctangent is ill defined. The values in deep blue where $\theta \cong 0$ in all the polarization plots should therefore be ignored as they are negligible contributions to the measured polarization and are the result of the high pass $|\vec{E}|$ filter.

$$\theta = \tan^{-1} \left(\frac{|E_r|}{|E_z|} \right) * (|\vec{E}| > 5 \times 10^4 \text{ V/m}) \quad (2)$$

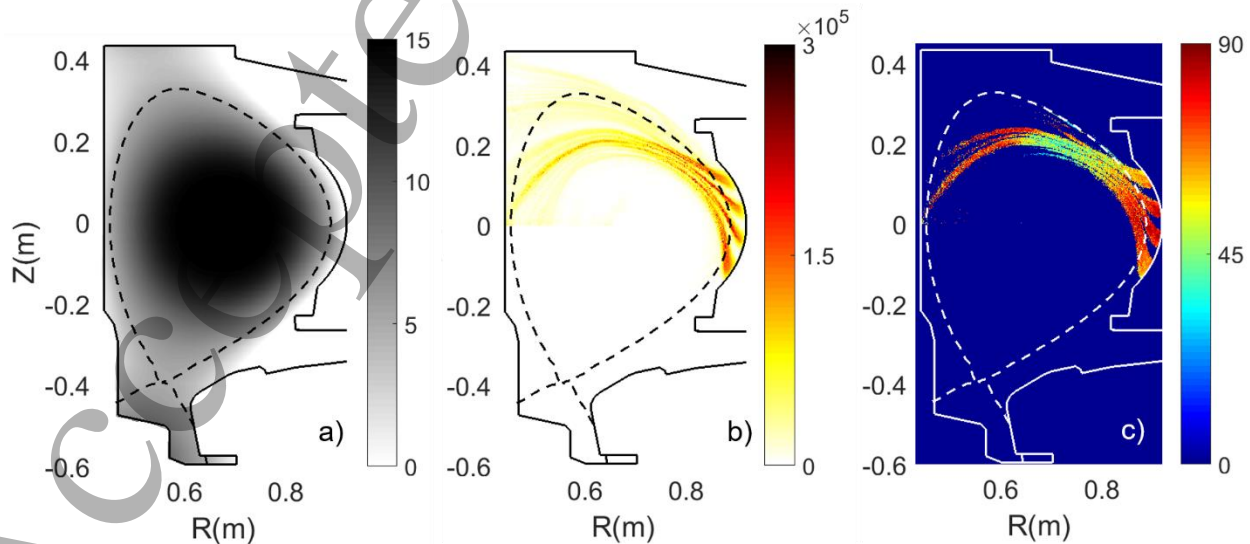


Figure 1. a) Density profile (10^{19} m^{-3}) without fluctuations is shown for an example input into the full wave model. b) Output $|\vec{E}|$ (V/m) is shown. c) Output θ (degrees) is shown. The dashed black lines in a), b) and dashed white line in c) is the last closed flux surface (LCFS). The solid black lines in a), b), and solid white line in c) is the vacuum vessel geometry.

2.2 3-D SELHF synthetic diagnostic

The SELHF diagnostic has a 3-D viewing geometry so a 3-D model of the LH electric fields is necessary as a synthetic diagnostic. A 3-D model of the LH electric field is achieved by a summation of many 2-D axisymmetric simulations in equation (1) over many toroidal mode numbers or parallel wavenumbers. This is shown in equation (3) where φ is toroidal coordinate, and A_m is the amplitude of the vacuum toroidal mode spectrum of the launched LH waves. A_m is calculated by taking the Fourier transform of the 16 columns of the LH launcher by assuming the electric field at each column of the mouth of the waveguide is a rectangular function with relative waveguide phasing of 90° . Details of this calculation are shown in reference 42 and a figure of the parallel wavenumber spectrum on Alcator C-Mod is shown in reference 43.

$$\vec{E}(r, z, \varphi) = \sum_m A_m \vec{E}_m(r, z) e^{im\varphi} \quad (3)$$

KN1D neutral modeling⁴⁴ and realistic sightline geometry is used to post-process the 3-D result for direct comparison to SELHF diagnostic. KN1D calculates the neutral atomic and molecular deuterium profiles in slab-like geometry with input plasma profiles, radial location of limiters, and the molecular neutral pressure at the wall. The neutral pressure is measured by an ionization gauge and was approximately 0.06 Pa at the main chamber for this experiment. The radial location of the limiter of Alcator C-Mod and the measured density and estimated temperature profile are used as inputs. While this 1-D geometry may not be suitable for 2-D problems such as divertors, it may be sufficient to simulate plasma-neutral interactions in the main chamber of a tokamak, such as the case of LH current drive in this paper. The major advantage of using KN1D is that it only takes a few seconds of computational time, which is useful when running many cases.

The comparison to the SELHF measurement is calculated in (4) where the integrals are evaluated over the sightline volume (dV), $|\vec{E}_\varphi|$, $|\vec{E}_{\perp r}|$, and $|\vec{E}_{\perp z}|$ are the amplitudes of the toroidal, radial, and vertical components of the LH electric fields calculated by the 3-D finite element model, and $E_{SELHF\varphi}$, $E_{SELHF\perp r}$, $E_{SELHF\perp z}$, and $|\vec{E}_{SELHF}|$, are the calculated LH electric fields to be compared to the measurements. θ_{SELHF} is the angle between the perpendicular components of the LH electric field. D_β is the deuterium Balmer line emission at wavelengths approximately equal to 486 nm with transitions from the principal quantum number of 4 to 2.

$$E_{SELHF\varphi} = \frac{\int |\vec{E}_\varphi| D_\beta dV}{\int D_\beta dV} \quad (4a)$$

$$E_{SELHF\perp r} = \frac{\int |\vec{E}_{\perp r}| D_\beta dV}{\int D_\beta dV} \quad (4b)$$

$$E_{SELHF\perp z} = \frac{\int |\vec{E}_{\perp z}| D_{\beta} dV}{\int D_{\beta} dV} \quad (4c)$$

$$|\vec{E}_{SELHF}| = \sqrt{E_{SELHF\phi}^2 + E_{SELHF\perp r}^2 + E_{SELHF\perp z}^2} \quad (4d)$$

$$\theta_{SELHF} = \tan^{-1} \left(\frac{E_{SELHF\perp r}}{E_{SELHF\perp z}} \right) \quad (4e)$$

An example 3-D simulation is shown in figure 2. There is substantial toroidal and poloidal variation of the LH electric field. Because of the cosine dependence of the TE₁₀ mode of the LH waveguides, the electric field peaks at the center of each row of the waveguide and goes to zero at the top and bottom of each waveguide. There are therefore 4 distinct rows of $|\vec{E}|$ observed poloidally in figure 2a), consistent with the 4 rows of the LH launcher. As the LH electric field propagates radially inwards and toroidally away from the LH launcher, it gets absorbed and consequently $|\vec{E}|$ decreases. It can be observed that the $|\vec{E}|$ is sharply peaked near the LH launcher and localized to a narrow region spatially. The synthetic diagnostic can capture these toroidal and poloidal variations accurately within the sightline geometry; this is shown in the $|\vec{E}|$ over one of the SELHF views near the LH launcher in figure 2b). An image of the LH launcher and some of the possible the SELHF views are also shown. For this paper, all the measurement and simulation focuses on a view a few cm toroidally outwards of the LH limiter and at the top-middle row of the LH launcher.

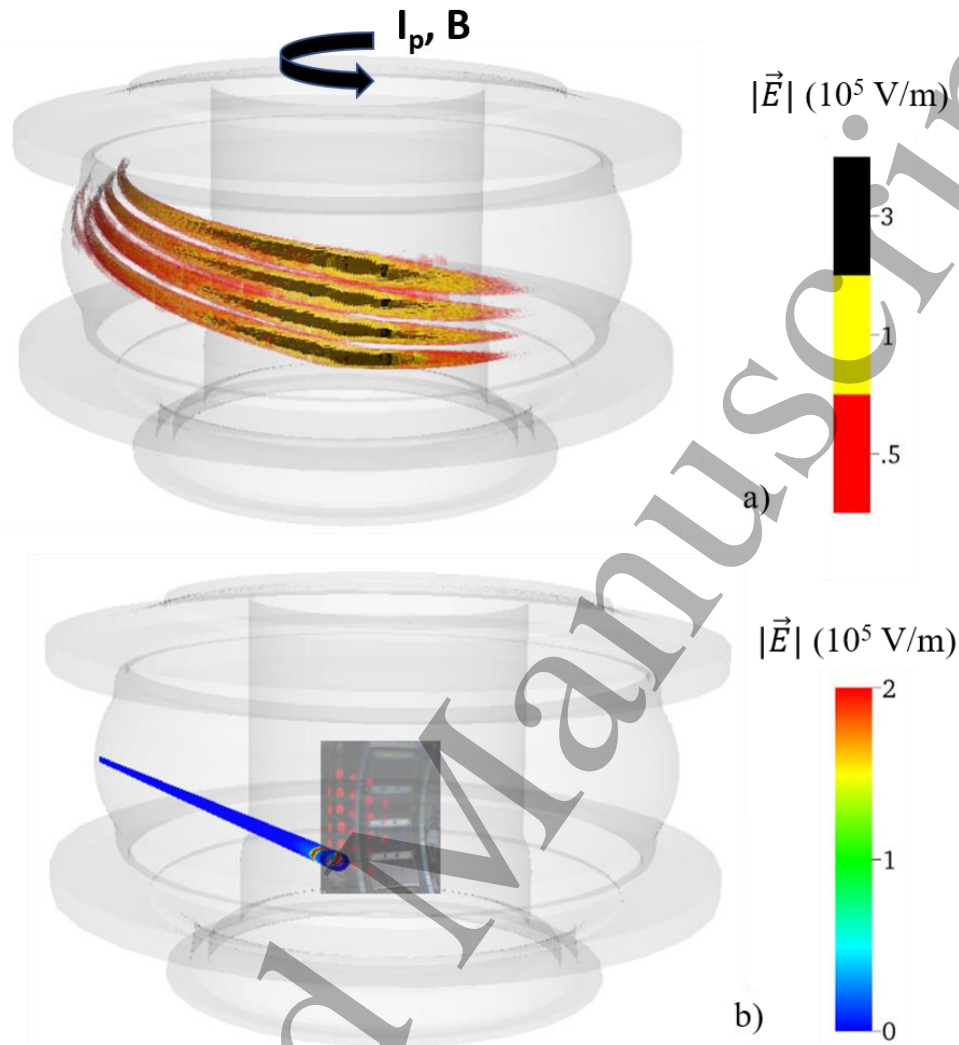


Figure 2. a) A 3-D image of $|\vec{E}|$. b) 3-D image of $|\vec{E}|$ over a viewing geometry of the SELHF diagnostic. The LH launcher is viewed from the back in this figure. The plasma current and magnetic field are counterclockwise when viewed from the top of the tokamak.

2.3 Sensitivity scan for the SELHF synthetic diagnostic

The most sensitive inputs to the SELHF synthetic diagnostic are the collision frequency and density. Figure 3 shows the simulated results for $|\vec{E}_{SELHF}|$ and θ_{SELHF} at different fixed values of ν/ω . The simulated $|\vec{E}_{SELHF}|$ is shown in figure 3a). The simulated θ_{SELHF} is shown in figure 3b). By varying the collision frequency by more than a factor of 5, the simulated $|\vec{E}_{SELHF}|$ can vary by approximately 30% at all location. $|\vec{E}_{SELHF}|$ is therefore somewhat sensitive to the collision frequency. For the scanned range of collision frequency, θ_{SELHF} varies by approximately 3° and is relatively insensitive to the collision frequency. At the lower range of scanned ν/ω , there appears to be numerical noise that prevents even lower values of ν/ω from being computed here.

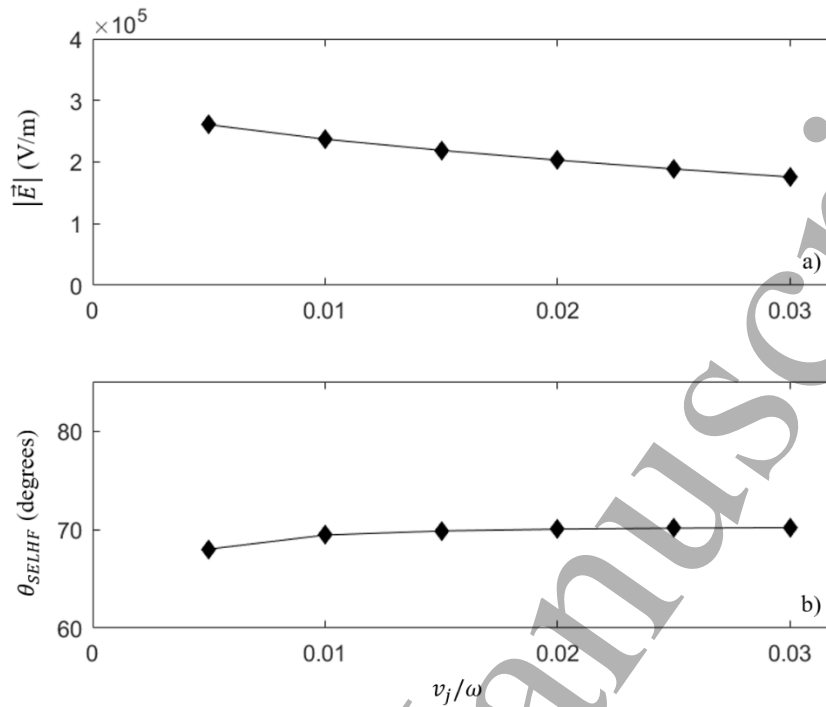


Figure 3. a) The simulated $|\vec{E}_{SELHF}|$ is shown for a range of collision frequencies. b) The simulated θ_{SELHF} is shown for a range of collision frequencies.

Figure 4 shows the simulated results for $|\vec{E}_{SELHF}|$ and θ_{SELHF} as a function of density. This is done by multiplying the density profile in figure 1 by a constant multiplicative factor, C . C ranges from .2 to 2 in figure 4. This variation is somewhat outside the error bars of the density profile measurement and is used to illustrate how $|\vec{E}_{SELHF}|$ depends strongly on density but θ_{SELHF} depends weakly on density. As can be observed, a factor of 10 change in the density profile results in close to a factor of 10 change in $|\vec{E}_{SELHF}|$. On the other hand, a factor of 10 change in the density profile only results in θ_{SELHF} changing by approximately 3° out of a measurement of 70° .

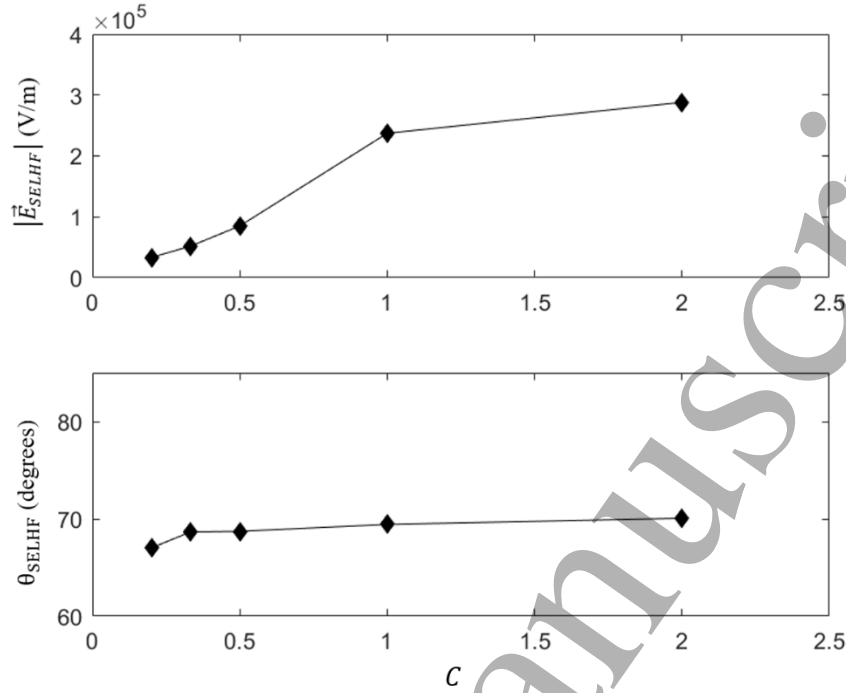


Figure 4: a) The simulated $|\vec{E}_{SELHF}|$ is shown for possible errors in the reflectometry density profile as a function of C , which is a multiplicative factor in the density profile. b) The simulated θ_{SELHF} is also shown.

This result shows that agreement between measurement and simulation for $|\vec{E}_{SELHF}|$ can be obtained within the associated uncertainties. On the other hand, the measured and simulated θ_{SELHF} do not agree within the associated uncertainties. This paper therefore focuses on understanding if and how synthetic turbulence can obtain better agreement for θ_{SELHF} between measurement and modeling.

2.4 Synthetic turbulence

The three synthetic turbulence models chosen for this paper are shown here in equation (5) where

$$n = n_{nf} \times \left[\left(1 + \frac{\tilde{n}}{n_{nf}} \times e^{-\frac{(p-p_c)^2}{\rho_w^2}} \times \cos\left(\frac{\pi(z-z_c)}{\lambda_{fluct}}\right) \times F(z) \right) \right] \text{ where} \quad (5a)$$

$$1 \quad (5b)$$

$$F(z) = \begin{cases} H\left[z - z_c + \frac{\lambda_{fluct}}{2}\right] \times H\left[z_c + \frac{\lambda_{fluct}}{2} - z\right] & (5c) \end{cases}$$

$$\begin{cases} -H\left[z - z_c + \frac{\lambda_{fluct}}{2}\right] \times H\left[z_c + \frac{\lambda_{fluct}}{2} - z\right] & (5d) \end{cases}$$

$H[x]$ is the Heaviside function. The case with no synthetic turbulence occurs when $F(z) = 0$. The synthetic turbulence in (5b) is representative of a periodic fluctuation, synthetic turbulence in (5c) is representative of a blob, and the synthetic turbulence in (5d) is representative of a hole⁴⁵ in the literature. A blob is an increase of density in a narrow region while a hole is a decrease in density in a narrow region.

For the rest of this paper, these turbulence models in equations (5b), (5c), and (5d) are referred to as periodic, blob, and hole, respectively. The density profile does not depend on time because the fluctuation frequency is much smaller than the LH frequency, so that the turbulence is effectively “frozen” in the timescale of the LH wave. This density profile is approximately based on experimental observations^{46,47} and simulation results⁴⁸ on Alcator C-Mod. It assumes a relatively large poloidal mode number with cosine periodicity poloidally that is controlled by the fluctuation wavelength, λ_{fluct} . p is the square root of the normalized toroidal flux. \tilde{n}/n controls the amplitude of the density fluctuations. There are also parameters (z_c, p_c, p_w) that control the poloidal location, radial location, and radial width of the turbulence. This simple synthetic turbulence equation is not intended to accurately simulate SOL turbulence, but to provide a simple parametrization of whether turbulent-driven poloidally asymmetric density profiles can modify the LH electric fields in a different manner compared to the cases without fluctuations.

This 2-D assumption for the synthetic turbulence does not contain any toroidal variation in the density. This may be a good physics approximation given that the toroidal variation of the fluctuations and LH wave may be much smaller than the radial and poloidal variations. LH-driven density striations are observed 180° away toroidally on magnetic field lines connected to the LH launcher⁴⁹. The parallel fluctuation wavelength for ballooning modes is estimated to be $2\pi qR$ ⁴⁸, which is greater than 10 m on Alcator C-Mod. This is much larger than radial and poloidal wavelengths, which on the order of a few centimeters⁴⁶. The lower hybrid toroidal wavelength is also usually much larger than the poloidal and radial wavelength⁵⁰. The assumption that the density and magnetic field profile are axisymmetric may therefore be justified with respect to turbulence length scales.

3. Effect of synthetic turbulence on LH wave propagation

This section is intended to illustrate the LH wave scattering and interference that can occur because of turbulence on LH waves. Examples using the 2-D axisymmetric model are presented for the case without fluctuations, blob-like fluctuations, hole-like fluctuations, and periodic fluctuations in sections 3.1, 3.2, 3.3, and 3.4, respectively to highlight the effect to turbulence. \tilde{n}/n and λ_{fluct} will be modified in this section.

The other parameters are chosen to be constant for this paper, mostly for simplicity. The radial location of the fluctuations is chosen just outside the last closed flux surface. The radial width of the fluctuations is approximately 1 cm. The poloidal location is near a high $|\vec{E}|$ region. Variations in these parameters can quantitatively affect these results. However, if the fluctuations are near a high $|\vec{E}|$ regions, similar qualitative results occur. While the simulation is carried out with the full vacuum vessel geometry, the figures are zoomed into a small region in the SOL where the pertinent dynamics of the interactions of turbulence and LH waves are located. This region is also the region where the SEHLF diagnostic measures due to the high D_β emission in the near and far SOL as compared to the core plasma.

3.1 Effect of density profile without fluctuations on LH wave propagation

For comparison purposes to the cases with fluctuations, the case without fluctuations is shown. Figure 5 a) to c) shows the density profile, $|\vec{E}|$, and θ in a zoomed-in region near the outer midplane of the SOL on Alcator C-Mod for the same simulation case in figure 1. The density profile is radially monotonic and constant on the flux surface and the LH $|\vec{E}|$ propagates in a typical resonance cone with no scattering or interference patterns. The $|\vec{E}|$ propagates smoothly into the core plasma. θ is relatively uniform during the high $|\vec{E}|$ regions at approximately 70°.

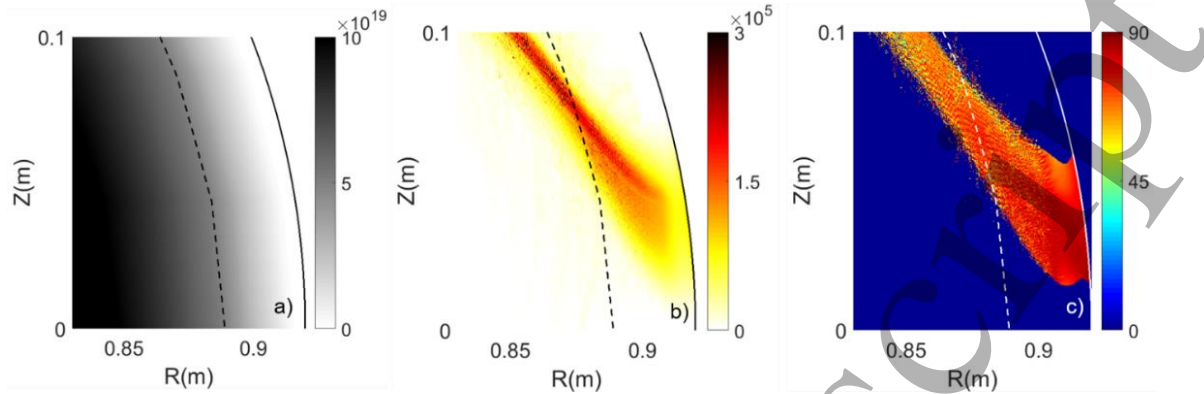


Figure 5. a) Density profile without fluctuations (m^{-3}) is shown for an example input into the full wave model. b) Output $|\vec{E}|$ (V/m) is shown. c) Output θ (degrees) is shown. The dashed black lines in a), b) and dashed white line in c) is the last closed flux surface (LCFS). The solid black lines in a), b), and solid white line in c) is the vacuum vessel geometry.

3.2 Effect of blobs on LH wave propagation

When fluctuations are added, the results can differ substantially from figure 5. Figure 6 a) to l) details the density profiles, $|\vec{E}|$, and θ with the addition of a single blob for four different λ_{fluct} of 0.25, 0.5, 3, and 25 cm. $\tilde{n}/n = 0.8$ for all these cases. Each row of figure 6 corresponds to a different λ_{fluct} with the first row at the smallest λ_{fluct} and the last row at the largest λ_{fluct} . The density blob at different λ_{fluct} just outside the LCFS is clearly observed in the density profile in figure 6 a), d), g), and j). Depending on λ_{fluct} , there could be backscattering of the waves due to the blob. This is observed in the $|\vec{E}|$ profile in figure 6 b) or e) or side scattering of the LH waves observed in figure 6 h) and k). Significant fractions of the desired incident LH wave does not propagate into the core, particularly for the cases with shorter poloidal wavelengths. Differences in the LH \vec{E} occur particularly for $\lambda_{fluct} = 0.25$ or 0.5 cm while $\lambda_{fluct} = 25$ cm seems to have the least impact on the LH resonance of the 4 cases. Wave interference and strong SOL $|\vec{E}|$ occur near the blob, likely due to the interaction between the incident and scattered LH wave. This interference seems to have a strong dependence on λ_{fluct} . For the regions with strong interference and/or scattering, the polarization of the LH wave can also be modified significantly, as observed in figure 6 c), f), i), and l). θ of the backscattered LH wave appears to be 40-50°, which is about 20-30° lower than the incident LH wave shown in figure 5.

The amplitude of the fluctuations is also important. Figure 7 a) to l) details the density profiles, $|\vec{E}|$, and θ with the addition of a single blob for four different \tilde{n}/n of 0.2, 0.4, 0.6, and 0.8. $\lambda_{fluct} = 0.5$ cm for all these cases. Each row of figure 7 corresponds to a different \tilde{n} with the first row at the smallest fluctuation amplitude and the last row at the largest amplitude. The amplitude of the density fluctuation can also be observed in the density profile in figure 7 a), d), g) and j). For $\tilde{n} = 0.2$, the impact of the turbulence on the LH wave is barely noticeable in figure 7 b) and is very similar to the no fluctuation case in figure 5 b). As \tilde{n}/n increases, interference and backscattering gradually becomes more noticeable on the wave $|\vec{E}|$ as observed in figure 7 b), e), h), and k). Similarly, the polarization modifications at these regions become more noticeable in figure 7 c), f), i), and l). Increasing \tilde{n}/n clearly makes the effects of the blob on the LH electric field more noticeable and decreases the coupling of the LH wave to the core plasma as more of the LH wave becomes backscattered.

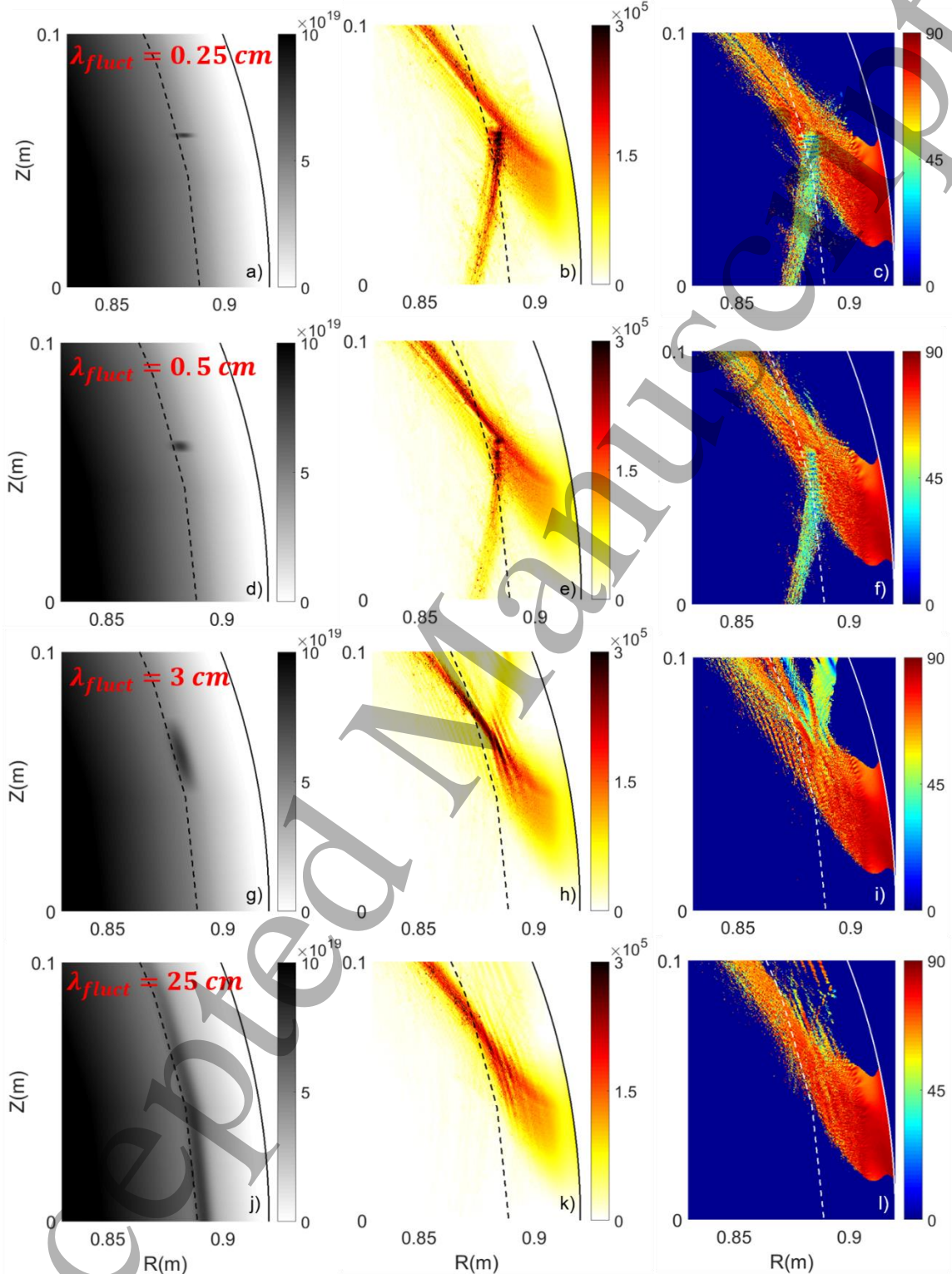


Figure 6. a)-c) Blob-like turbulent density profile (m^{-3}), $|\vec{E}|$ (V/m) is shown. c) Output θ (degrees) is shown for $\lambda_{fluct} = 0.25$ cm. d)-f). Same as a)-c) except for $\lambda_{fluct} = 0.5$ cm. g)-i). Same as a)-c) except for $\lambda_{fluct} = 3$ cm. j)-l). Same as a)-c) except for $\lambda_{fluct} = 25$ cm. $\tilde{n}/n = 0.8$ for all these cases.

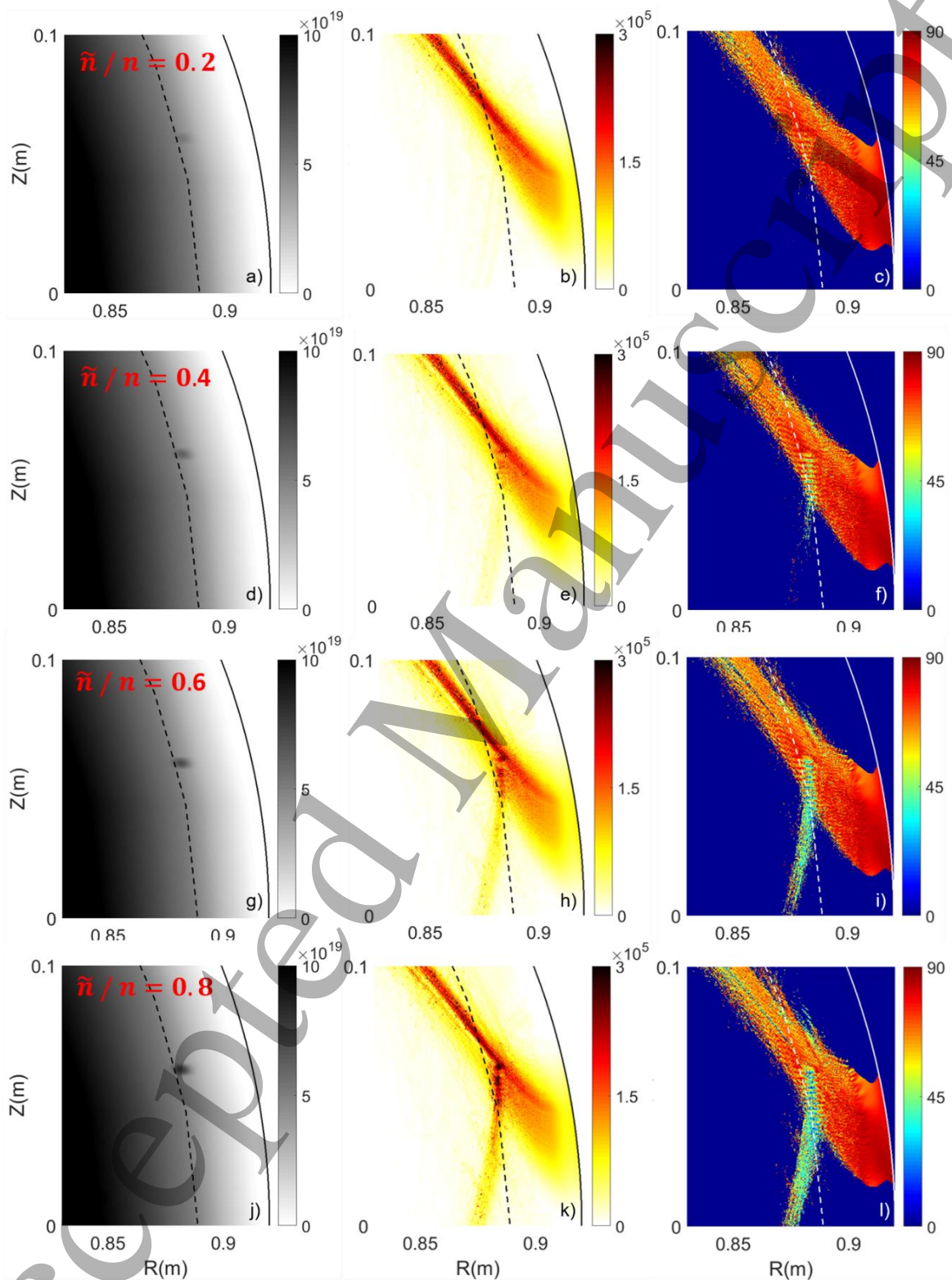


Figure 7. a)-c) Blob-like turbulent density profile (m^{-3}), $|\vec{E}|$ (V/m) is shown. c) Output θ (degrees) is shown for $\tilde{n}/n = 0.2$. d)-f). Same as a)-c) except for $\tilde{n}/n = 0.4$. g)-i). Same as a)-c) except for $\tilde{n}/n = 0.6$. j)-l). Same as a)-c) except for $\tilde{n}/n = 0.8$. $\lambda_{fluct} = 0.5$ cm for all these cases.

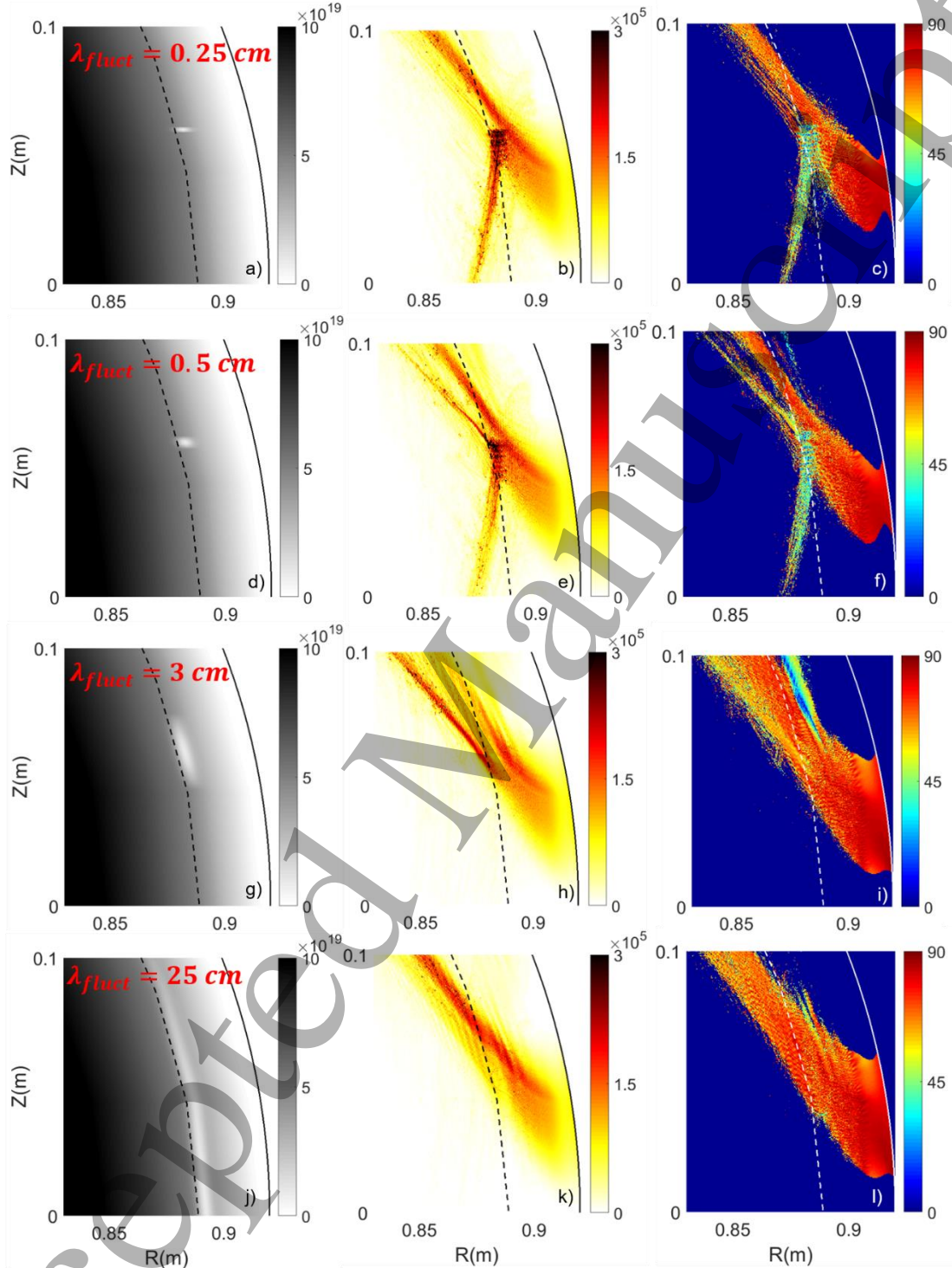


Figure 8. a)-c) Hole-like turbulent density profile (m⁻³), $|\vec{E}|$ (V/m) is shown. c) Output θ (degrees) is shown for $\lambda_{fluct} = 0.25$ cm. d)-f). Same as a)-c) except for $\lambda_{fluct} = 0.5$ cm. g)-i). Same as a)-c) except for $\lambda_{fluct} = 3$ cm. j)-l). Same as a)-c) except for $\lambda_{fluct} = 25$ cm. $\tilde{n}/n = 0.8$ for all these cases.

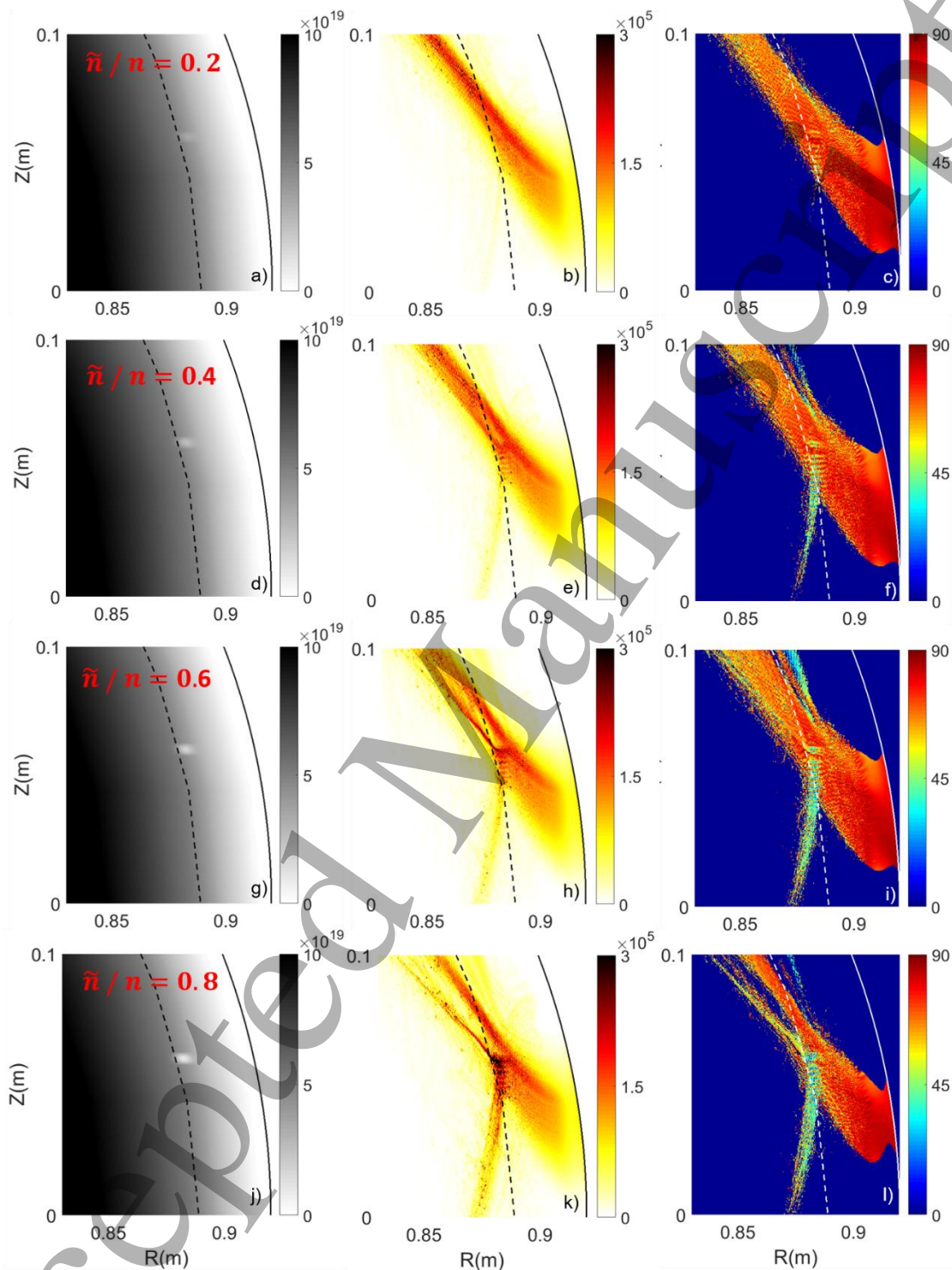


Figure 9. a)-c) Hole-like turbulent density profile (m^{-3}), $|\vec{E}|$ (V/m) is shown. c) Output θ (degrees) is shown for $\tilde{n}/n = 0.2$. d)-f). Same as a)-c) except for $\tilde{n}/n = 0.4$. g)-i). Same as a)-c) except for $\tilde{n}/n = 0.6$. j)-l). Same as a)-c) except for $\tilde{n}/n = 0.8$. $\lambda_{fluct} = 0.5$ cm for all these cases.

3.3 Effect of holes on LH wave propagation

Similar results are observed with a hole-like fluctuation. Figure 8 a) to l) and figure 9 a) to l) detail a fluctuation poloidal wavelength and amplitude scan similar to the blob-like fluctuation case in figures 6 and 7. The density profile due to the hole is shown in figure 8 a), d), g) and j) and 9 a), d), g), and j). The results are similar to the blob-like fluctuation case as wave backscattering, side scattering, and interference occur and has a strong dependence on λ_{fluct} , particularly for the smaller λ_{fluct} . Increasing \tilde{n} increases the effects of scattering and interference in both $|\vec{E}|$, and θ . Increasing \tilde{n}/n clearly makes the effects of the hole more noticeable and decreases the coupling of the LHCD to the core plasma as more of the LH wave becomes backscattered. θ of the backscattered LH wave appears to be between 40-50°, which is about 20-30° lower than the incident LH wave. One difference between the effects of blobs versus holes on the LH wave is that the incident LH wave fields seem to diverge and go around the hole-like fluctuation while the wave fields appear to converge for the blob-like fluctuation. Otherwise, the resulting LH wave backscattered, and side scattered fields are remarkably similar for a hole versus a blob for each fluctuation poloidal wavelength and amplitude.

3.4 Effect of periodic fluctuations on LH wave propagation

The periodic fluctuations are shown in figures 10 and 11 for a fluctuation poloidal wavelength and amplitude scan similar to the blob-like and hole-like fluctuations. The qualitative pattern appears different at small wavelengths compared to the blob-like and hole-like fluctuations; the effects of interference and possibly diffraction are much more noticeable, especially at small wavelengths for figures 10 e) and h). The LH wave does not couple to the core plasma and is mostly contained in the SOL where regions of low and high $|\vec{E}|$ can occur due to diffraction. The polarization modifications at the interference patterns in figures 10 f) and i) are also prominent. In the periodic fluctuations, however, the polarization modification is mainly prominent at the location of the fluctuation and not at locations far away from the fluctuation, as observed in a backscattered wave. The scattering of the LH wave still exists but may be partially masked by the large effects of the LH wave interference and diffraction. At large wavelengths, there is some interference and scattering, similar to the previous results for blob-like and hole-like fluctuations. For the amplitude scan at small wavelengths, there are clear signs that for increasing \tilde{n}/n , wave interference and diffraction at the fluctuation becomes more noticeable and modifies $|\vec{E}|$ decreases θ significantly at the interference patterns. $|\vec{E}|$ increases and decrease depending on the phase of the interference pattern.

It is therefore clear for each of the three different synthetic turbulence profiles, the fluctuations can modify the LH wave, particularly when the amplitude of the fluctuations is large, and the poloidal fluctuation wavelength is small. It is interesting that for all three synthetic turbulence profile, the largest response of the LH wave appears at the same poloidal fluctuation wavelength of approximately 0.5 cm. The LH wavelength is approximately 0.5 cm in this discharge at this location and this may indicate that strong scattering and interference occurs when the LH wavelength is close to the fluctuation wavelength. The propagation of the LH wave therefore appears sensitive to the poloidal fluctuation wavelength but not very sensitive to the poloidal fluctuation profile. However, at larger poloidal fluctuation wavelengths and smaller fluctuation amplitudes, the effect of turbulence on LH waves is minimal. To understand if fluctuations can be a realistic effect in the Alcator C-Mod experiment, it is necessary to compare the simulated θ with those measured by SELHF.

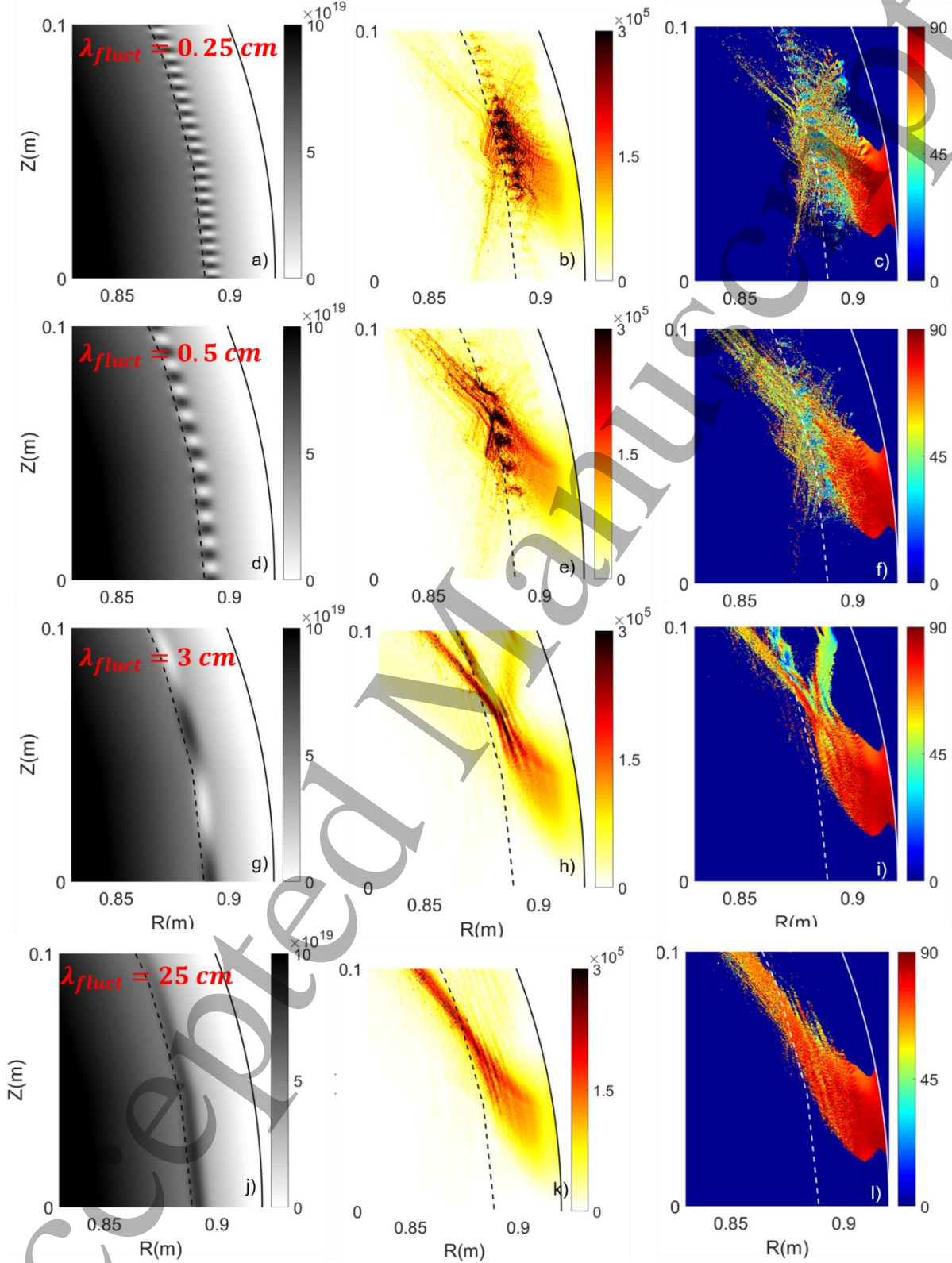


Figure 10. a)-c) Periodic-like turbulent density profile (m^{-3}), $|\vec{E}|$ (V/m) is shown. c) Output θ (degrees) is shown for $\lambda_{fluct} = 0.25$ cm. d)-f). Same as a)-c) except for $\lambda_{fluct} = 0.5$ cm. g)-i). Same as a)-c) except for $\lambda_{fluct} = 3$ cm. j)-l). Same as a)-c) except for $\lambda_{fluct} = 25$ cm. $\tilde{n}/n = 0.8$ for all these cases.

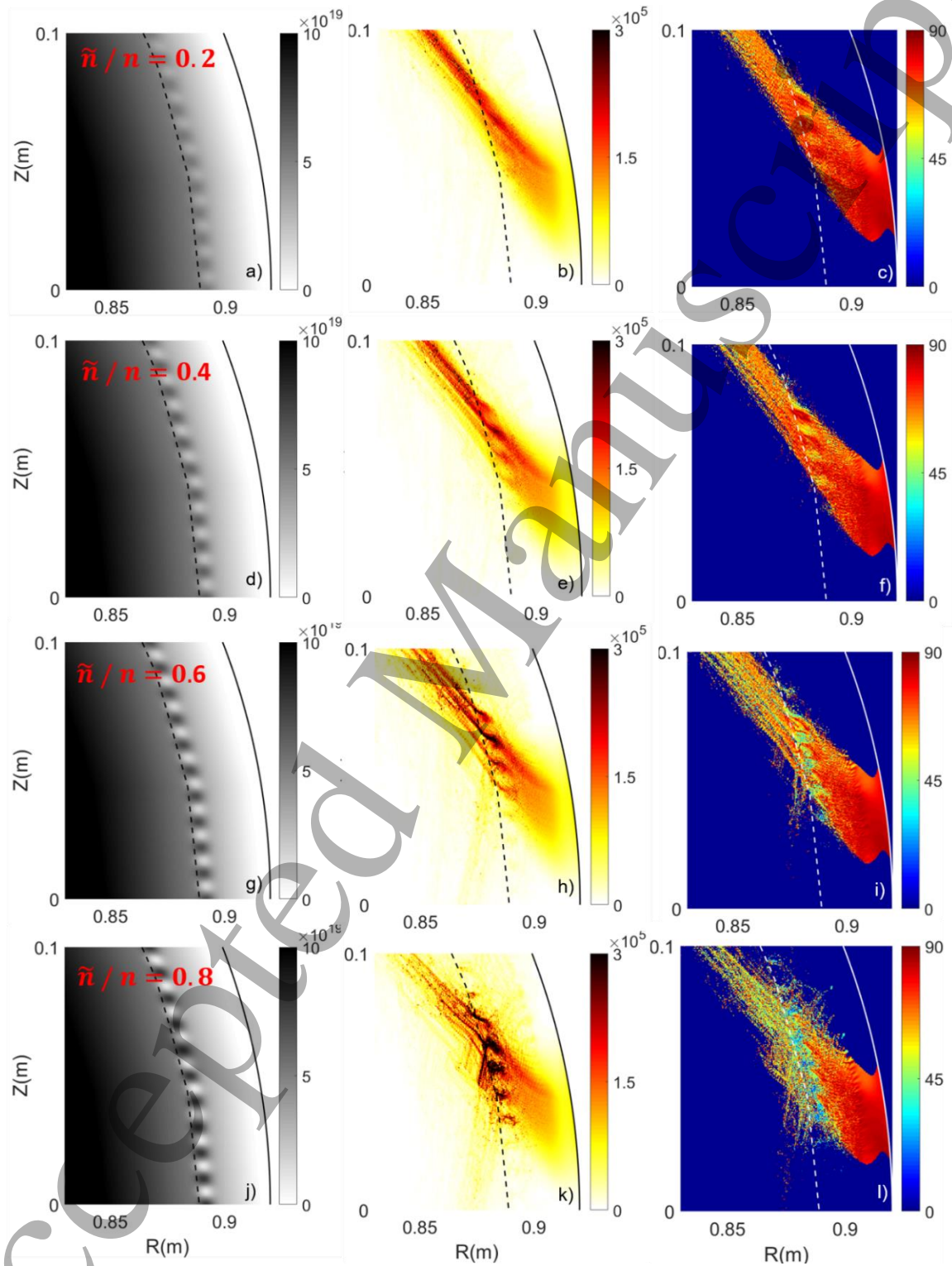


Figure 11. a)-c) Periodic-like turbulent density profile (m^{-3}), $|\vec{E}|$ (V/m) is shown. c) Output θ (degrees) is shown for $\tilde{n}/n = 0.2$. d)-f). Same as a)-c) except for $\tilde{n}/n = 0.4$. g)-i). Same as a)-c) except for $\tilde{n}/n = 0.6$. j)-l). Same as a)-c) except for $\tilde{n}/n = 0.8$. $\lambda_{fluct} = 0.5$ cm for all these cases.

4. Impact of fluctuations on LH polarization and LH SOL fractional power losses

This section will evaluate the impact of density fluctuations on LH polarization and SOL power losses. This is shown in sections 4.1 and 4.2, respectively.

4.1 Effect of fluctuations on LH polarization

Figure 12 shows an example comparison between the measured LH polarization (black shaded region) and the simulated LH polarization (red circle) for different periodic fluctuation amplitudes at $\lambda_{fluct} = 1$ cm. \tilde{n}/n was not measured and there was only one θ_{SELHF} measurement for this set of conditions so the black shaded error bars represent the SELHF measurement and measurement uncertainty in θ_{SELHF} and \tilde{n}/n . θ_{SELHF} can be modified by about 20° or so depending on the amplitude of the fluctuations. For $\lambda_{fluct} = 1$ cm, the inclusion of synthetic turbulence at large amplitudes ($\tilde{n}/n > 0.8$) agree reasonably well with experimental results. The hole-like and blob-like fluctuations also generally see decreases in θ_{SELHF} with increasing \tilde{n}/n and smaller wavelengths, but not to as large of an extent as the periodic fluctuations. The periodic fluctuations are also chosen for simplicity because they are not as sensitive to the radial and poloidal location of the blob-like and hole-like fluctuations and therefore require less parameters to scan.

This differs significantly from the results without synthetic turbulence in figures 3 and 4 where θ_{SELHF} remains essentially unchanged within approximately 3 degrees for a wide range of density profiles and collision frequencies. With $\tilde{n}/n < 0.5$ or small levels of turbulence, the discrepancy between the measured and simulated θ_{SELHF} could not be resolved. This is true for cases where the density profile is assumed constant on the flux surface shown in this paper or for cases not shown here where the density profile may be poloidally asymmetric due to LH driven ExB drifts⁵¹.

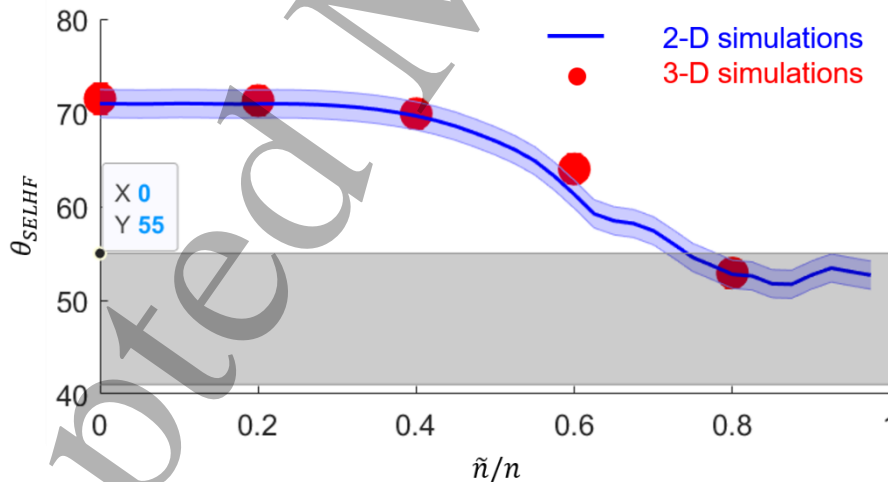


Figure 12. 2-D (blue line) at a dominant toroidal mode number and 3-D (red circle) simulation results averaging over many toroidal mode numbers are shown as a function of fluctuation amplitude. The measurement is shown by the black diamond. The blue shaded error bars is the estimated $\pm 1.5^\circ$ uncertainty based on the results of the sensitivity scan for collisions and density in figures 3 and 4. There is only one θ_{SELHF} measurement for this set of conditions and the black shaded error bars represent the measurement uncertainty in θ_{SELHF} and \tilde{n}/n .

Figure 12 also shows a comparison between 2-D axisymmetric simulations (blue line) versus a 3-D simulation (red circle). For simplicity, averaging over a 4 cm long square box centered radially at the fluctuations and poloidally at the center of the LH resonance cone is assumed to estimate θ_{SELHF} in the 2-

D simulations. The 3-D simulations accurately calculate θ_{SELHF} based on the realistic sightline geometry. The difference between the 2-D and 3-D simulations is surprisingly small. Using 2-D simulations therefore appears to be a reasonable assumption to understand the trends of θ_{SELHF} with various fluctuation parameters. This is done for the rest of the paper because the computational resources for the full 3-D synthetic diagnostic is substantial and prevent large parametric studies.

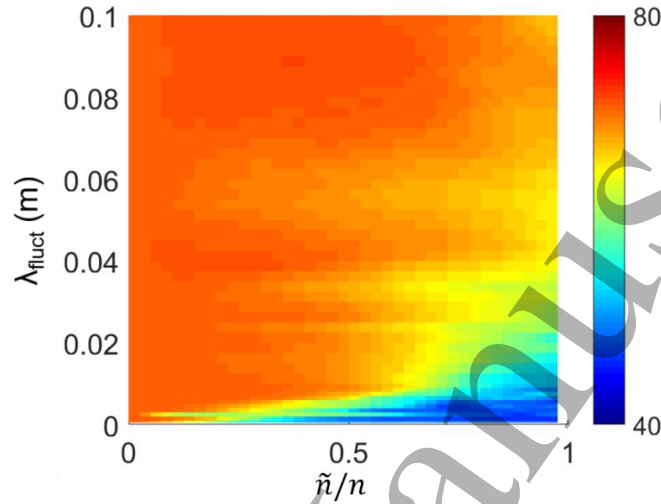


Figure 13. θ_{SELHF} for a parametric scan of \tilde{n}/n and λ_{fluct}

One of these parametric scans is shown in Figure 13 where θ_{SELHF} is calculated for a range of \tilde{n}/n and λ_{fluct} . There are strong dependencies on θ_{SELHF} as a function of \tilde{n}/n and λ_{fluct} . On average, θ_{SELHF} decreases for increasing \tilde{n}/n and decreasing λ_{fluct} , similar to the results of section 3. The polarization ranges from around 45° to 70° over this wide range of \tilde{n}/n and λ_{fluct} . Given that the measurement is between 40° and 55°, high $\tilde{n}/n > 0.5$ and low $\lambda_{fluct} \sim 0.1$ to 1 cm appear necessary for the simulation to match experiment.

4.2 Effect of fluctuations on LH SOL absorption

Figure 14 shows the SOL power absorption fraction (f_{SOL}) that is absorbed outside the LCFS for a parametric scan of \tilde{n}/n and λ_{fluct} using the periodic fluctuation case with a single toroidal mode number of 170. f_{SOL} is calculated using equation (6) where \vec{J} is the current and ρ is the normalized magnetic flux.

$$f_{SOL} = \frac{\int (\vec{J} \cdot \vec{E}) * (\rho > 1) dV}{\int (\vec{J} \cdot \vec{E}) dV} \quad (6)$$

On average, f_{SOL} increases for increasing \tilde{n}/n and decreasing λ_{fluct} . Moreover, f_{SOL} has similar structure and appears to be anti-correlated to θ_{SELHF} as a function of \tilde{n}/n and λ_{fluct} . This is particularly evident for large \tilde{n}/n and small λ_{fluct} . It should be noted that the quantitative value of f_{SOL} here is strongly dependent on the collision frequency and density profile. However, the trends of f_{SOL} with \tilde{n}/n and λ_{fluct} are independent of the collision frequency and density profile, so this anti-correlation should be robust to a wide range of relevant SOL density and temperature profiles.

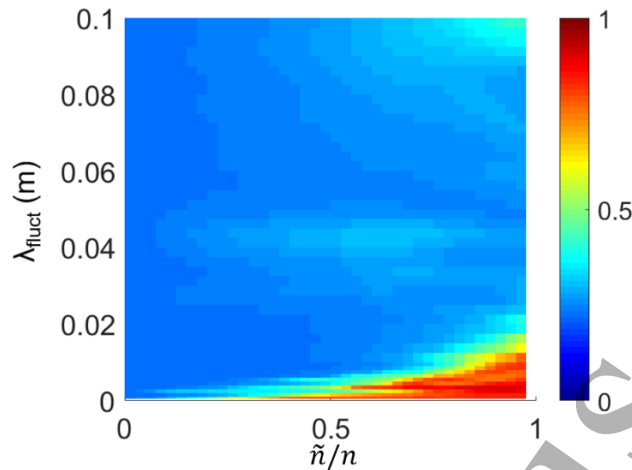


Figure 14. f_{SOL} for a parametric scan of \tilde{n}/n and λ_{fluct}

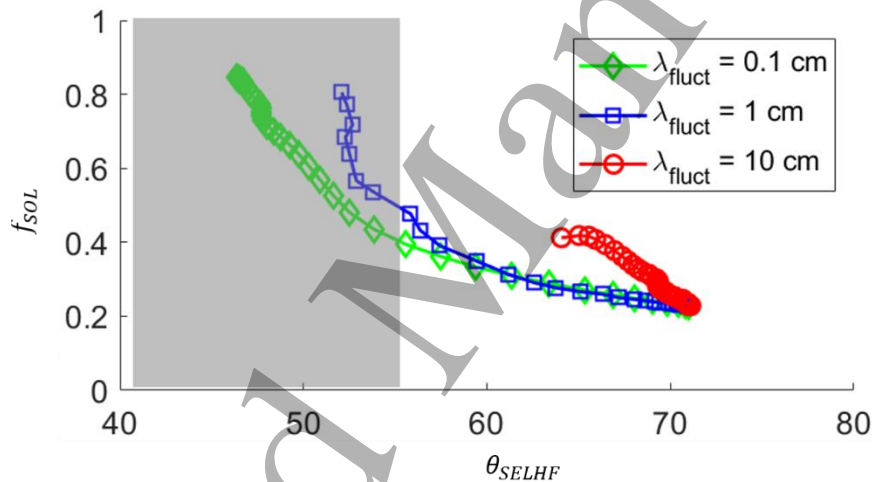


Figure 15. f_{SOL} versus θ_{SELHF} for three different λ_{fluct} . The individual values for each λ_{fluct} represent the different \tilde{n}/n values that were scanned. There is only one θ_{SELHF} measurement for this set of conditions and the black shaded error bars represent the measurement uncertainty in θ_{SELHF} and \tilde{n}/n .

Figure 15 shows this anti-correlation between f_{SOL} and θ_{SELHF} more clearly for three different λ_{fluct} over a wide range of \tilde{n}/n . The individual values for each λ_{fluct} represent the different \tilde{n}/n values that were scanned. For all three λ_{fluct} , it appears that there is an inverse relationship between f_{SOL} and θ_{SELHF} . When the LH polarization is modified, more power is absorbed in the SOL. The exact details for this structure and anti-correlation is not clear, but it has also been recently observed experimentally on Alcator C-Mod that the amplitude of SOL turbulence appear anti-correlated with LHCD efficiency²³. These simulations are therefore consistent with the experimental observations for LH polarization modifications and reduced LHCD efficiency at large SOL fluctuation amplitudes.

5. Discussion and conclusion

A cold plasma full wave model has been developed as a synthetic diagnostic for a LH electric field magnitude and polarization measurement. The synthetic diagnostic can match experimental measurements for the LH electric field magnitude but cannot match measurement for the LH electric field polarization²⁷.

1
2
3
4 The first key result of this paper is that the inclusion of poloidally varying density fluctuations with the
5 appropriate amplitude and poloidal wavelength in the model can greatly modify the LH wave propagation
6 and absorption for a range of synthetic turbulence models such as periodic, blobs, and holes. While there
7 are some differences depending on the synthetic turbulence model, a poloidal fluctuation wavelength of \sim
8 0.1 to 1 cm and a fluctuation amplitude ($\tilde{n}/n > 0.5$) results in strong LH polarization modifications for all
9 the synthetic turbulence models. The LH wavelength is approximately 0.5 cm and this appears consistent
10 with previous known results^{50,52} where there may be strong scattering when the LH wavelength is close to
11 the fluctuation wavelength.
12

13
14 The second key result is that the inclusion of synthetic turbulence can allow for better agreement
15 between experimental measurement and simulation of the LH polarization. The physical mechanism for
16 LH polarization modifications appear to be due to some combination of backscattering, interference, and/or
17 diffraction effects. These effects are discussed in detail in simpler models using cylindrical density
18 filaments^{53,54}. Because of the backward nature of the LH slow wave, there can be significant backscattering
19 as well as forward and side scattering. This is evident particularly for the hole and blob case where the wave
20 clearly backscatters with a significant polarization modification. Interference and diffraction effects are also
21 important, particularly given the large changes of the LH polarization in periodic lobes in the periodic case.
22 Many previous efforts^{25,55-58} on LH polarization modifications uses the ray tracing technique, which cannot
23 capture interference and diffraction effects. Full wave effects therefore are important to understanding LH
24 polarization.
25

26
27 The third key result is that the calculated SOL absorption of the LH wave and polarization modification
28 are anti-correlated. These results support previous arguments that SOL density fluctuations are important
29 in understanding LH propagation and absorption²³⁻²⁵ and anti-correlated with LHCD efficiency with
30 increased fluctuation levels²³ at increasing Greenwald density fraction⁵⁹. Fluctuations may therefore be
31 important in understanding the observed SOL absorption of LH waves, particularly at high line averaged
32 densities. Launching at a region with significantly lower density fluctuation amplitudes such as the high
33 field side of a tokamak⁶⁰ may therefore be beneficial for increased LHCD efficiency at high densities.
34

35 One important factor to better understand the influence of SOL density fluctuations on LHCD
36 efficiency is that these full wave models use a cold plasma approximation. A kinetic tensor along with
37 appropriate models such as CQL3D⁶¹ to capture current drive and non-thermal behavior are necessary
38 improvements for a full wave model. Improvements on existing hot-plasma ray-tracing code could be
39 considered. While ray tracing cannot capture diffraction or interference effects, assumptions may be
40 possible to mimic these effects. Fourier transform of the cold-plasma full wave model in the SOL could
41 provide appropriate perpendicular wavenumbers as initial conditions into ray-tracing codes. Prior work
42 largely focused on a “tail model” that introduces spectral broadening in n_{\parallel} , largely to understand the
43 “spectral gap” problem. More recent work has investigated the use of spectral broadening in the
44 perpendicular wavenumber⁶².
45

46 Other important features to better understand density fluctuations on LH polarization, propagation, and
47 absorption are a better turbulence model and high time resolution density profile and density fluctuation
48 measurement will be important. The results of sections 3 and 4 clearly indicate that the LH polarization and
49 absorption profile is sensitive to the fluctuation amplitude and wavelength. While previous work^{47,63} has
50 suggested that the synthetic turbulence model may be somewhat reasonable, a predictive physics model
51 will better constrain the inputs to the 3-D full wave model.
52

53 Acknowledgements

54
55
56
57
58
59
60

The authors will like to acknowledge Naoto Tsujii for help with 3-D visualization, R. Michael Churchill for help with KN1D, and Robert Mumgaard (Commonwealth Fusion Systems) for help with some of the measurements and experiments. The authors will also like to acknowledge Paul Bonoli (MIT), Andris Dimits (LLNL), David Green (ORNL), Maxim Umansky (LLNL), and John Wright (MIT) for helpful discussions on coupling turbulence with plasma wave modeling. This work was supported by U.S. Department of Energy, Office of Science, Office of Fusion Energy Sciences under contract numbers DE-AC05-00OR22725 and DE-FC02-99ER54512. This material is based upon work supported by the US Department of Energy, Office of Science, Office of Fusion Energy Sciences under contract number DE-AC05-00OR22725. This manuscript has been authored in part by UT-Battelle, LLC, under contract DE-AC05-00OR22725 with the US Department of Energy (DOE). The US government retains and the publisher, by accepting the article for publication, acknowledges that the US government retains a nonexclusive, paid-up, irrevocable, worldwide license to publish or reproduce the published form of this manuscript, or allow others to do so, for US government purposes. DOE will provide public access to these results of federally sponsored research in accordance with the DOE Public Access Plan (<http://energy.gov/downloads/doe-public-access-plan>).

References

1. Najmabadi, F. *et al.* The ARIES-I Tokamak Reactor Study [†]. *Fusion Technol.* **19**, 783–790 (1991).
2. Maisonnier, D. *et al.* Power plant conceptual studies in Europe. *Nucl. Fusion* **47**, 1524–1532 (2007).
3. Konishi, S., Nishio, S. & Tobita, K. DEMO plant design beyond ITER. *Fusion Eng. Des.* **63–64**, 11–17 (2002).
4. Ekedahl, A. *et al.* Long distance coupling of lower hybrid waves in JET plasmas with edge and core transport barriers. *Nucl. Fusion* **45**, 351–359 (2005).
5. Bécoulet, A. *et al.* Steady state long pulse tokamak operation using Lower Hybrid Current Drive. *Fusion Eng. Des.* **86**, 490–496 (2011).
6. Pericoli-Ridolfini, V. *et al.* High plasma density lower-hybrid current drive in the ftu tokamak. *Phys. Rev. Lett.* **82**, 93–96 (1999).
7. Cesario, R. *et al.* Current drive at plasma densities required for thermonuclear reactors. *Nat. Commun.* **1**, 1–8 (2010).
8. Wallace, G. M. *et al.* Absorption of lower hybrid waves in the scrape off layer of a diverted tokamak. *Phys. Plasmas* **17**, 082508 (2010).
9. Shiraiwa, S. *et al.* Progress towards steady-state regimes in Alcator C-Mod. *Nucl. Fusion* **53**, 113028 (2013).
10. Wan, B., Li, J., Guo, H., Liang, Y. & Xu, G. Progress of long pulse and H-mode experiments in EAST. *Nucl. Fusion* **53**, 104006 (2013).
11. Ding, B. J. *et al.* Investigations of LHW-plasma coupling and current drive at high density related to H-mode experiments in EAST. *Nucl. Fusion* **55**, 093030 (2015).
12. Wallace, G. M. *et al.* Lower hybrid current drive at high density in the multi-pass regime. *Phys. Plasmas* **19**, 62505 (2012).
13. Goniche, M. *et al.* Lower hybrid current drive at high density on Tore Supra. *Nucl. Fusion* **53**, 033010 (2013).
14. Wallace, G. M. *et al.* Lower hybrid current drive at high density in Alcator C-Mod. *Nucl. Fusion* **51**, 083032 (2011).
15. Faust, I. C. *et al.* Lower hybrid wave edge power loss quantification on the Alcator C-Mod tokamak. *Phys. Plasmas* **23**, 056115 (2016).
16. Cesario, R. *et al.* Spectral broadening of lower hybrid waves produced by parametric instability in current drive experiments of tokamak plasmas. *Nucl. Fusion* **46**, 462–476 (2006).
17. Napoli, F., Castaldo, C., Cesario, R. & Schettini, G. Modeling of the nonlinear mode coupling of

- 1
2
3 lower hybrid waves in tokamak plasmas. *Plasma Phys. Control. Fusion* **55**, (2013).
- 4 18. Baek, S. G. *et al.* Measurements of ion cyclotron parametric decay of lower hybrid waves at the
5 high-field side of Alcator C-Mod. *Plasma Phys. Control. Fusion* **55**, 052001 (2013).
- 6 19. Zhao, A. & Gao, Z. Parameter study of parametric instabilities during lower hybrid wave injection
7 into tokamaks. *Nucl. Fusion* **53**, (2013).
- 8 20. Cesario, R. *et al.* Spectral broadening of parametric instability in lower hybrid current drive at a
9 high density. *Nucl. Fusion* **54**, (2014).
- 10 21. Faust, I. C. *et al.* Lower hybrid wave edge power loss quantification on the Alcator C-Mod
11 tokamak. *Phys. Plasmas* **23**, 056115 (2016).
- 12 22. Castaldo, C. *et al.* Influence of collisions on parametric instabilities induced by lower hybrid
13 waves in tokamak plasmas. *Nucl. Fusion* **56**, (2016).
- 14 23. Baek, S. G. *et al.* Observation of Efficient Lower Hybrid Current Drive at High Density in
15 Diverted Plasmas on the Alcator C-Mod Tokamak. *Phys. Rev. Lett.* **121**, 055001 (2018).
- 16 24. Ridolfini, V. P. *et al.* Lower hybrid current drive efficiency in tokamaks and wave scattering by
17 density fluctuations at the plasma edge. *Nucl. Fusion* **51**, 113023 (2011).
- 18 25. Peysson, Y., Decker, J., Morini, L. & Coda, S. RF current drive and plasma fluctuations. *Plasma*
19 *Phys. Control. Fusion* **53**, 124028 (2011).
- 20 26. Madi, M., Peysson, Y., Decker, J. & Kabalan, K. Y. Propagation of the lower hybrid wave in a
21 density fluctuating scrape-off layer (SOL). *Plasma Phys. Control. Fusion* **57**, 125001 (2015).
- 22 27. Martin, E. H., Lau, C., Wallace, G. M., Shiraiwa, S. & Mumgaard, B. Experimental evidence of
23 lower hybrid wave scattering in Alcator C-Mod due to scrape off layer density fluctuations. *Nucl.*
24 *Fusion* (2019). doi:10.1088/1741-4326/ab16a2
- 25 28. Martin, E. H. *et al.* Electric field determination in the plasma-antenna boundary of a lower-hybrid
26 wave launcher in Tore Supra through dynamic Stark-effect spectroscopy. *Plasma Phys. Control.*
27 *Fusion* **57**, 065011 (2015).
- 28 29. Wallace, G. M. *et al.* Advances in lower hybrid current drive technology on Alcator C-Mod. *Nucl.*
29 *Fusion* **53**, 73012 (2013).
- 30 30. Wright, J. C. *et al.* Full wave simulations of fast wave mode conversion and lower hybrid wave
31 propagation in tokamaks. *Phys. Plasmas* **11**, 2473–2479 (2004).
- 32 31. Hillairet, J. *et al.* ALOHA: an Advanced Lower Hybrid Antenna coupling code. *Nucl. Fusion* **50**,
33 125010 (2010).
- 34 32. Klepper, C. C. *et al.* Dynamic Stark Spectroscopic Measurements of Microwave Electric Fields
35 Inside the Plasma Near a High-Power Antenna. *Phys. Rev. Lett.* **110**, 215005 (2013).
- 36 33. Shiraiwa, S. *et al.* Plasma wave simulation based on a versatile finite element method solver. *Phys.*
37 *Plasmas* **17**, 056119 (2010).
- 38 34. Meneghini, O., Shiraiwa, S. & Parker, R. Full wave simulation of lower hybrid waves in
39 Maxwellian plasma based on the finite element method. *Phys. Plasmas* **16**, 090701 (2009).
- 40 35. Stix, T. H. & Howard, T. Waves in plasmas. *Waves plasmas*, by Stix, Thomas Howard.; Stix,
41 Thomas Howard. New York Am. Inst. Physics, c1992. (1992).
- 42 36. Lao, L. L. *et al.* MHD equilibrium reconstruction in the DIII-D tokamak. *Fusion Sci. Technol.* **48**,
43 968–977 (2005).
- 44 37. Lau, C. *et al.* First results of the SOL reflectometer on Alcator C-Mod. *Rev. Sci. Instrum.* **83**,
45 10E309 (2012).
- 46 38. Lau, C. *et al.* AORSA full wave calculations of helicon waves in DIII-D and ITER. *Nucl. Fusion*
47 (2018).
- 48 39. Bertelli, N. *et al.* Effect of the scrape-off layer in AORSA full wave simulations of fast wave
49 minority, mid/high harmonic, and helicon heating regimes. in *AIP Conference Proceedings* **1689**,
50 30010 (2015).
- 51 40. Lau, C., Berry, L. A., Jaeger, E. F. & Bertelli, N. Cold plasma finite element wave model for
52 helicon waves. *Plasma Phys. Control. Fusion* **61**, 045008 (2019).
- 53 41. Brambilla, M. Slow-wave launching at the lower hybrid frequency using a phased waveguide
54
55
56
57
58
59
60

- array. *Nucl. Fusion* **16**, 47–54 (1976).
42. Wallace, G. M. Behavior of lower hybrid waves in the scrape off layer of a diverted tokamak. (2010).
43. Bonoli, P. T. *et al.* Lower hybrid current drive experiments on Alcator C-Mod: Comparison with theory and simulation. *Phys. Plasmas* **15**, 056117 (2008).
44. Labombard, B. *KNID: A 1-D space, 2-D velocity, kinetic transport algorithm for atomic and molecular hydrogen in an ionizing plasma.* (2001).
45. Xu, G. S. *et al.* Blob/hole formation and zonal-flow generation in the edge plasma of the JET tokamak. *Nucl. Fusion* **49**, 092002 (2009).
46. Terry, J. L. *et al.* Observations of the turbulence in the scrape-off-layer of Alcator C-Mod and comparisons with simulation. *Phys. Plasmas* **10**, 1739–1747 (2003).
47. Zweben, S. J. *et al.* Comparison of edge turbulence imaging at two different poloidal locations in the scrape-off layer of Alcator C-Mod. *Phys. Plasmas* **20**, 072503 (2013).
48. Grulke, O., Terry, J. L., Cziegler, I., LaBombard, B. & Garcia, O. E. Experimental investigation of the parallel structure of fluctuations in the scrape-off layer of Alcator C-Mod. *Nucl. Fusion* **54**, 043012 (2014).
49. James, A. N. *et al.* Imaging of molybdenum erosion and thermography at visible wavelengths in Alcator C-Mod ICRH and LHCD discharges. *Plasma Phys. Control. Fusion* **55**, 125010 (2013).
50. Bonoli, P. T. Toroidal and scattering effects on lower-hybrid wave propagation. *Phys. Fluids* **25**, 359 (1982).
51. Lau, C. *et al.* Effects of LH power on SOL density profiles and LH coupling on Alcator C-Mod. *Plasma Phys. Control. Fusion* **55**, 25008 (2013).
52. Ott, E. Lower hybrid wave scattering by density fluctuations. *Phys. Fluids* **22**, 1732 (1979).
53. Ram, A. K. & Hizanidis, K. Scattering of radio frequency waves by cylindrical density filaments in tokamak plasmas. *Phys. Plasmas* **23**, 022504 (2016).
54. Ioannidis, Z. C., Ram, A. K., Hizanidis, K. & Tigelis, I. G. Computational studies on scattering of radio frequency waves by density filaments in fusion plasmas. *Phys. Plasmas* **24**, 102115 (2017).
55. Ridolfini, V. P. *et al.* Study and optimization of lower hybrid wave coupling in advanced scenario plasmas in JET. *Plasma Phys. Control. Fusion* **46**, 349–368 (2004).
56. Bertelli, N. *et al.* The effects of the scattering by edge plasma density fluctuations on lower hybrid wave propagation. *Plasma Phys. Control. Fusion* **55**, 074003 (2013).
57. Decker, J. *et al.* Damping of lower hybrid waves in large spectral gap configurations. *Phys. Plasmas* **21**, 092504 (2014).
58. Ding, B. J. *et al.* Review of recent experimental and modeling advances in the understanding of lower hybrid current drive in ITER-relevant regimes. *Nucl. Fusion* **58**, 095003 (2018).
59. LaBombard, B. *et al.* Particle transport in the scrape-off layer and its relationship to discharge density limit in Alcator C-Mod. *Phys. Plasmas* **8**, 2107–2117 (2001).
60. Bonoli, P. T. *et al.* High field side lower hybrid wave launch for steady state plasma sustainment. *Nucl. Fusion* **58**, (2018).
61. Harvey, R. W. & McCoy, M. G. The cql3d fokker-planck code. *IAEA TCM Montr.* (1992).
62. S. G Baek, P. T. Bonoli, D. Brunner, I. C. Faust, A. E. Hubbard, J. W. Hughes, B. Labombard, R. R. Parker, M. Porkolab, A. Seltzman, S. Shiraiwa, G. M. Wallace, and S. J. W. Role of the Edge/Scrape-Off Layer in Lower Hybrid Current Drive Experiments on Alcator C-Mod. in *23rd RFPPC in Hefei* (2019).
63. Umansky, M. V., Rognlien, T. D. & Xu, X. Q. Simulation of turbulence in the divertor region of tokamak edge plasma. *J. Nucl. Mater.* **337–339**, 266–270 (2005).